Remote Sensing of Environment 139 (2013) 216–230

Contents lists available at ScienceDirect

Remote Sensing of Environment

journal homepage: www.elsevier.com/locate/rse

Validation of coarse spatial resolution LAI and FAPAR time series over cropland in southwest France

Martin Claverie [a,b,*], Eric F. Vermote [b], Marie Weiss [c], Frédéric Baret [c], Olivier Hagolle [d], Valérie Demarez [d]

[a] Department of Geographical Sciences, University of Maryland, College Park, MD 20742, USA
[b] NASA-Goddard Space Flight Center, Greenbelt, MD 20771, USA
[c] EMMAH, INRA-UMR 1114, Domaine Saint-Paul, Site Agroparc, 84914 Avignon, France
[d] CESBIO, UMR CNES-CNRS-IRD-UPS, 18, avenue Edouard Belin, 31401 Toulouse Cedex 4, France

ARTICLE INFO

Article history:
Received 23 April 2013
Received in revised form 22 July 2013
Accepted 23 July 2013
Available online xxxx

Keywords:
LAI
GAI
FAPAR
Essential Climate Variables
Green Area Index
Radiative transfer model
PROSAIL
MODIS
Formosat-2
Crop
Validation
Surface reflectance
BRDF

ABSTRACT

This study aims at validating Leaf Area Index (LAI) and Fraction of Absorbed Photosynthetically Active Radiation (FAPAR) products derived from MODIS surface reflectance (MOD09CMG) at coarse resolution (0.05°) over crops. These Essential Climate Variables (ECVs) are estimated by using the inversion of the PROSAIL radiative transfer (BV-NNET tool) applied on MODIS BRDF (Bidirectional Reflectance Distribution Function) corrected surface reflectances and non-corrected. ECV estimates and the corresponding MCD15A3 Collection 5 and GEOLAND-2 (GEOv1) products are compared with ECV reference maps derived from BV-NNET applied on 105 high spatial resolution images (Formosat-2, 8 m) which were acquired from 2006 to 2010 in Southwest France. These latter are compared with local scale in situ measurements. The validation shows an uncertainty of 0.35 and 0.07 for LAI and FAPAR, respectively.

The comparison shows that the ECV estimates from the three products properly capture the crops phenology in agreement with reference maps. Results indicate that MCD15A3 uncertainties (0.23 and 0.07 for LAI and FAPAR, respectively) are similar to previous intercomparison studies. GEOv1 shows a systemic positive bias for both LAI and FAPAR. The best agreement with the reference maps is found for MODIS BV-NNET products with r^2 higher than 0.9 and relative uncertainties lower than 17%. The use of BRDF-corrected surface reflectances as input of BV-NNET tool improves the uncertainty of LAI estimates (0.11, compared to 0.17 when directional surface reflectances are used as input) but not the uncertainty of FAPAR estimates. The deviation between FAPAR products which mostly affects low winter FAPAR, is related to the discrepancy of the soil directional assumption in PROSAIL model and BRDF correction method. The temporal stability of the daily MODIS BV-NNET products is better than the 4-day composite MCD15A3 products. Finally, BV-NNET tool applied at finer resolutions demonstrates that the increase of the resolution results in a decrease of the LAI and FAPAR uncertainties and a conservation of the biases.

1. Introduction

Leaf Area Index (LAI) and Fraction of Absorbed Photosynthetically Active Radiation (FAPAR) are known as key vegetation biophysical variables. LAI corresponds to one half the total green (i.e., photosynthetically active) leaf area per unit horizontal ground surface (GCOS, 2011). FAPAR quantifies the photosynthetic capacity of vegetation. These two biophysical variables were assigned by the Global Climate Observing System (GCOS) as Essential Climate Variables (ECVs). ECVs were defined as measurements of atmosphere, oceans, or land that are technically and economically feasible for systematic observation and have a high impact on the requirements of the United Nations Framework Convention on Climate Change (UNFCCC) and the Intergovernmental Panel on Climate Change (IPCC). The concept of ECV includes a wide panel of terrestrial variables. However, ECV refers in this paper to the two biophysical variables of concern: LAI and FAPAR. Vegetation processes (photosynthesis, transpiration, carbon assimilation and respiration) are strongly driven by the surface of the plant in contact with atmosphere. In land surface models, which are used to evaluate the role of vegetation in the context of global climate change and variability (Running et al., 1999), LAI and/or FAPAR play a key role, specifically with respect to the carbon and water cycles (GCOS, 2011). Hence, the GCOS and the Food and Agriculture Organization (FAO) highlighted the need of accurate LAI and FAPAR measurements from in situ and earth observation systems (GCOS, 2010; Gobron & Verstraete, 2009a, 2009b).

In this context, efforts have been achieved by the scientific community to provide rapid and reliable ECV estimates. Since the 80s, a variety of methods have been developed to retrieve ECVs from earth observation data using Radiative Transfer Models (RTM). RTM summarize our understanding of the physical laws governing the interaction between

* Corresponding author at: Department of Geographical Sciences, University of Maryland, College Park, MD 20742, USA.
E-mail address: martin.claverie@nasa.gov (M. Claverie).

0034-4257/$ – see front matter © 2013 Elsevier Inc. All rights reserved.
http://dx.doi.org/10.1016/j.rse.2013.07.027

solar radiation and the canopy. RTM allow simulating canopy reflectances from the leaf and canopy characteristics, as well as the background reflectance. Their complexity ranges from simple 1-D (i.e. turbid and homogenous medium) to 3-D representations (Ray-tracing) of the vegetation (Widlowski et al., 2008). Among them, the PROSAIL model, a 1-D RTM resulting from the combination of PROSPECT and SAIL (Scattering by Arbitrarily Inclined Leaves) models, has become one of the most popular and used RTM due to general robustness, consistent validation, as well as ease of use (Jacquemoud et al., 2009). However, retrieving ECVs implies using RTM in the inverse mode. Among the large number of existing retrieving inversion techniques (see Baret & Buis, 2008 for a complete review), Artificial Neural Networks (ANN) have received much attention since they can model complex non-linear and multivariate systems (e.g., Duveiller, Weiss, Baret, & Defourny, 2011; Sedano, Lavergne, Ibañez, & Gong, 2008; Verger, Baret, & Camacho, 2011; Vohland, Mader, & Dorigo, 2010; Walthall et al., 2004).

Taking benefit of the available earth observation data and the existing retrieval methods, the scientific community achieved an operational production of medium resolution ECV global maps. Among them, the MODIS LAI and FAPAR Collection 5 (MOD15, Myneni et al., 2002) products are derived from a 3-D RTM inversion (main algorithm) and a calibrated NDVI relationship (backup algorithm). ECVs are produced at 1 km spatial resolution daily and composited over an 8-day period based on the maximum FAPAR value. To account for more rapid change, a 4-day composite product has recently been released (MCD15A3). Products derived from other sensors and based on different inversion and compositing techniques, are also made available: GEOLAND-2 (GEOv1, Baret et al., accepted for publication), CYCLOPES (Baret et al., 2007) products are derived from the SPOT/VEGETATION reflectances, while the JRC-FAPAR (Gobron et al., 2006) uses MERIS data and GLOBCARBON (Deng, Chen, Plummer, Chen, & Pisek, 2006), a combination of VEGETATION and AATSR data.

Existing LAI and FAPAR products are all based on temporal composite (4 to 30-day windows period), while most of ECV algorithms (e.g. MOD15, CYCLOPES, JRC-FAPAR) are able to provide multiple instantaneous estimates rather than a unique composite estimate during the windows period. Over the years, climate modelers promoted using composite in order: (i) to fill potential gaps due for instance to cloud coverage, (ii) to reduce the residual noise associated to the data, and (iii) to reduce data volume. Composite gap-filled time series are particularly suitable for climate modelers, since LAI is generally not simulated by the models and used directly as an input variable, with no change of the model parameters. However, LAI is used in other model categories for which assimilation approaches could be different. As an example, LAI crop model assimilation is regularly based on parameterization approach (Rembold, Atzberger, Savin, & Rojas, 2013). This approach requires a maximum of input observation to estimate the parameters set which best describes the LAI dynamic, including sharp changes of surface, such as vegetation green-up or crop harvest. The parameterization approach does not required gap-filled time series as only valid data are used. The time series noise can be assessed by calculating the data assimilation residual (e.g., Fisher & Courtier, 1995) or by using statistical metrics (e.g., Vermote, Justice, & Breon, 2009). Finally, storage capacities have significantly improved within the past 10 years and are not a limit anymore for medium resolution data volume. It therefore appears adequate to provide, aside from existing compositing data, instantaneous products to users, which means daily data for most of the medium resolution sensors.

There is also a critical need to understand and quantify the uncertainties associated to these products (Morisette et al., 2006). In 2006, the GCOS identified target requirement uncertainties of 0.5 for LAI and 0.05 for FAPAR (GCOS, 2006). In 2011, they were updated to max(0.5, 20%) for LAI and max(0.05, 10%) for FAPAR (GCOS, 2011). The Land Product Validation (LPV) of the Committee on Earth Observation Satellites (CEOS) designed a hierarchical four-stage validation approach. Global medium resolution products (250 m–1 km) are considered to be validated on Stage 2 ("Spatial and temporal consistency of the product and with similar products has been evaluated over globally representative locations and time periods"). It has been performed over MODIS-15 (8-day composite), CYCLOPES, GLOBCARBON and ECOCLIMAP LAI and FAPAR by Weiss, Baret, Garrigues, and Lacaze (2007), Garrigues et al. (2008) and more recently by McCallum et al. (2010) and Camacho, Cernicharo, Lacaze, Baret, and Weiss (accepted for publication) who includes GEOv1. To perform an inter-comparison at global scale, some of these studies used the same CEOS LAI inter-comparison dataset (Morisette et al., 2006). Since performing ground measurement at medium spatial resolution is challenging, the product absolute uncertainty was assessed using a reduced number of sites (between 50 and 100). For each of these sites, a dedicated methodology was based on the combination of a High Spatial Resolution (HSR) image, such as SPOT or Landsat, and ground measurements achieved with a stratified sampling strategy (Cohen & Justice, 1999). Best global LAI uncertainties (Root Mean Square Deviation, RMSD) were found between 0.75 (GEOv1, Camacho et al., accepted for publication) and 1.4 (GLOBCARBON, Garrigues et al., 2008), depending on the study. Even if cropland in situ measurements were under-represented in the database, their associated uncertainty is the lowest as compared to other vegetation types. Concerning FAPAR, the RMSD was around 0.07 for GEOv1, and up to 0.22 for JRC-FAPAR (Camacho et al., accepted for publication). Consequently, these uncertainties did not match the GCOS specifications requirement ($\pm$0.5 for LAI and $\pm$0.05 for FAPAR). Moreover, Weiss et al. (2007) and Garrigues et al. (2008) concluded to the lack of in situ measurements and satellite imageries to evaluate the "temporal consistency" as set out in Stage 2 definition. Indeed, due to the low temporal resolution of HSR sensors, only 1 or 2 reference maps were derived per year and sites (except 4 for one site), which is not enough to evaluate the consistency of the LAI and FAPAR temporal trajectory. The recent availability of high spatial and temporal resolution Formosat-2 (F2, launched in 2004) sensor provides a good opportunity to evaluate coarse resolution products over time. Indeed, F2 is able to deliver daily 8 m spatial resolution data using a constant viewing angle thanks to an orbit with a 1-day repeat cycle.

This study evaluated the uncertainty of coarse resolution LAI and FAPAR products over cropland as well as their consistency over time. The study was thus achieved at the Climate Modeling Grid (CMG, 0.05 degree resolution in the geographic projection). The data processing and the validation strategy are summarized in the diagram of Fig. 1. First, we developed two products based on Artificial Neural Networks learned on PROSAIL simulations using the BV-NNET tool: ECV_{NET_MOD09} is estimated from MODIS directional surface reflectance (SR) data (MOD09CMG), while ECV_{NET_MODN} uses nadir-corrected SR data as inputs. The correction of the SR directional effects was performed with the VJB model (Bréon & Vermote, 2012; Vermote et al., 2009). Then, reference maps were generated by using BV-NNET applied on the high spatial and temporal resolutions sensor F2, and validated through direct comparison with in situ measurements performed throughout the season over three major crops of the area. Finally, these 8 m reference maps were upscaled to CMG and used for a direct comparison with coarse resolution ECV products previously introduced (ECV_{NET_MODN} and ECV_{NET_MOD09}) and two existing products: ECV_{MOD15} (referring to the MODIS-15 LAI and FAPAR Collection 5 products) and ECV_{GEOv1} (referring to the GEOv1 LAI and FAPAR products).

2. Study site and data description

The study area is located near Toulouse, in the Southwest of France (1°20′ E, 43°45′ N, Fig. 2). Croplands cover 50% of the study area. The remaining 50% corresponds to urban area (city of Toulouse in the northeast), forest, natural vegetation, and water bodies. The southeastern and the western parts of the study area are hilly landscapes with small fields (approximately 10 ha) and covered by non-irrigated crops (mainly wheat, rapeseed and sunflower). The center of the study area,

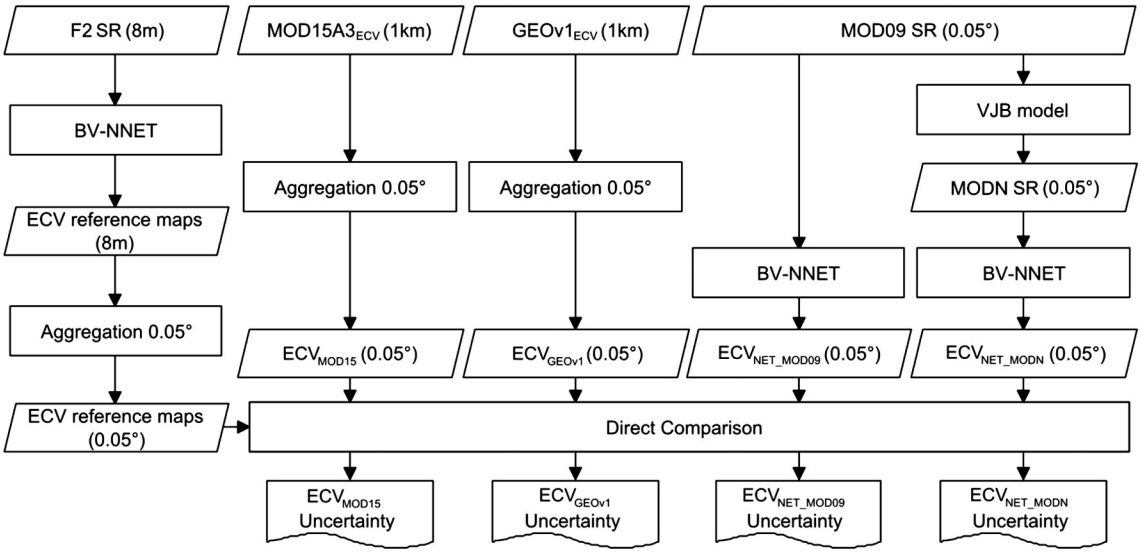

Fig. 1. Data processing and validation strategy diagram. SR stands for surface reflectance and ECV relate to the two biophysical variables of interest: LAI and FAPAR.

near the Garonne River, is generally flat with larger fields (approximately 25 ha) and covered by a mix of irrigated (mainly maize and soybean) and non-irrigated crops (mainly sunflower, wheat and rapeseed).

Field data were collected over 7 fields (3 maize, 2 sunflower and 2 soybean) land sampled 6 to 10 times (52 measurements in total) during summer of 2008. Among the variety of in situ measurement techniques

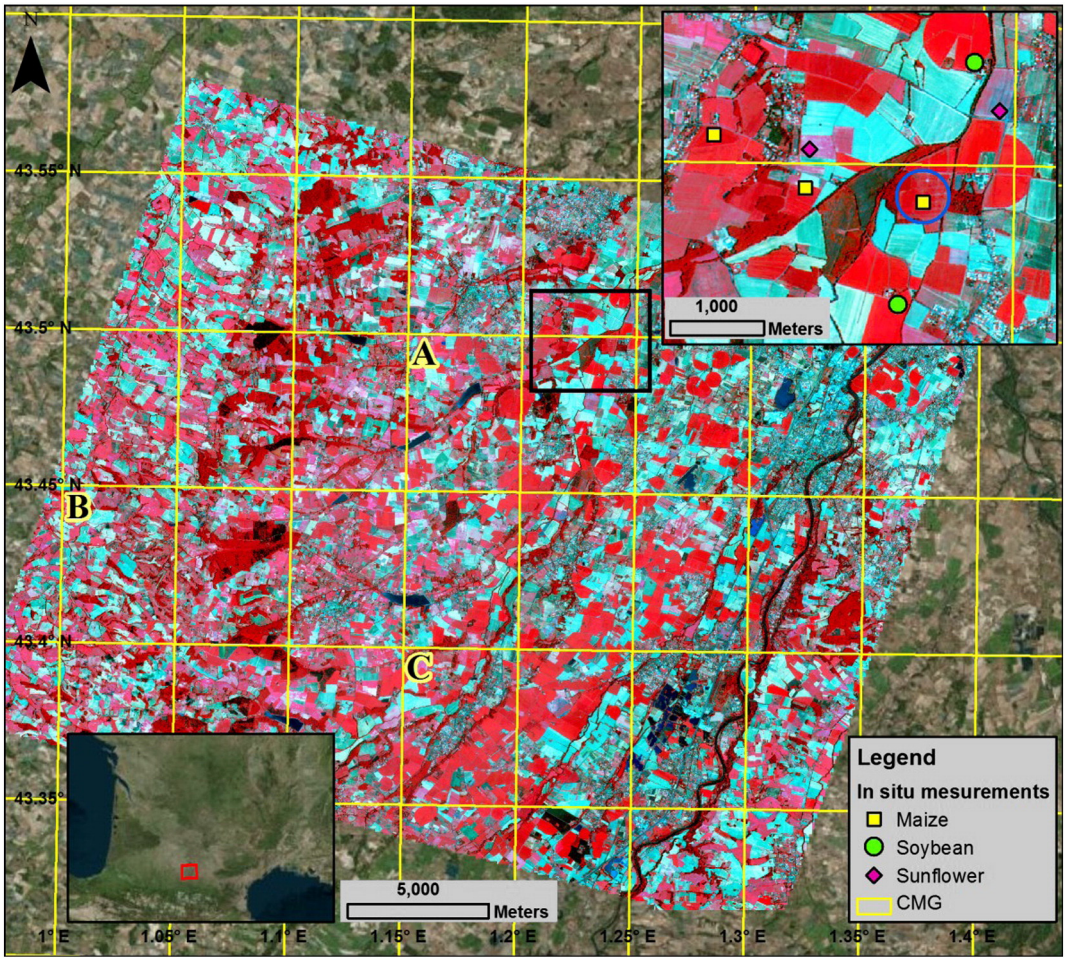

Fig. 2. Map of the study area, delimited by the Formosat-2 footprint. The displayed image corresponds to a color composite (bands 4–3–2) of Formosat-2 image acquired on 31-Jul-2008. Maize, sunflower and soybean fields where in situ measurements were performed in 2008 are represented in the upper-right frame. The blue circle is centered on the meteorological station used to compute diffuse fraction of incoming radiation. Yellow boxes display the extent of Climate Modeling Grid (CMG) pixels. A, B and C letters refer to selected pixels of Fig. 10. (For interpretation of the references to color in this figure legend, the reader is referred to the web version of this article.)

(see review of Weiss, Baret, Smith, & Jonckheere, 2004), Digital Hemispherical Photographs (DHPs, Demarez, Duthoit, Baret, Weiss, & Dedieu, 2008) were used to estimate LAI and FAPAR. Thirteen DHPs were sampled over an Elementary Sampling Unit (ESU), which corresponds to a 20 m × 20 m area located in a homogenous zone within the field. Each ESU was sampled with 13 DHPs by applying the VALERI spatial sampling protocol (http://w3.avignon.inra.fr/valeri). In our study, the DHPs were acquired with a calibrated Nikon CoolPix 8400 camera equipped with a FC-E8 fisheye lens. The camera was put at the top of a pole to keep the viewing direction (looking downward) and the canopy-to-sensor distance constant (~1.5 m) throughout the growing season (Demarez et al., 2008). The DHPs were processed using CAN-EYE V6.2 (http://www4.paca.inra.fr/can-eye), which provides estimates of the effective LAI, the true LAI, the daily direct and diffuse FAPAR (Baret, de Solan, Lopez-Lozano, Ma, & Weiss, 2010; Demarez et al., 2008). Comparison with destructive LAI over cropland provided mean differences of 0.63 and 0.56 for effective and true LAI, respectively (Demarez et al., 2008). The effective LAI was used for this study as it is highly correlated with remote sensing observations (Claverie et al., 2012). The daily FAPAR was computed from direct and diffuse components and diffuse fraction of incoming PAR (Photosynthetically Active Radiation) measured with a BF2 (Delta-T, Cambridge, UK, Béziat et al. 2009) located in an instrumented field (blue circle in Fig. 2).

The in situ measurements were combined with the acquisition of optical remote sensing data from Formosat-2 (F2, Chern & Wu, 2004). F2 is a high spatial (8 m) and temporal (daily revisit time) resolution satellite with four spectral bands (488, 555, 650 and 830 nm) and a field of view of 24 km. For a given site, F2 data may be acquired every day under a constant viewing angle. This characteristic was used to perform accurate atmospheric corrections by estimating the aerosol optical thickness using a multi-temporal method (Hagolle et al., 2008). All F2 images were first pre-processed for geometric, radiometric and atmospheric corrections (Hagolle et al., 2008) as well as cloud and cloud-shadow filtering (Hagolle, Huc, Pascual, & Dedieu, 2010). The final output product provides SR images and contains cloud and cloud/shadow masks. The absolute location accuracy is better than 0.4 pixel, i.e. 3.2 m (Baillarin, Gigord, & Hagolle, 2008), which is quite satisfactory with respect to the ESU size. A total amount of 105 images were acquired on the study area from 2006 to 2010, with different temporal distribution over the years: in 2006, 27 cloud and shadow-free (>85%) images out of 51 were available, while from 2007 to 2010, only 11 to 19 images per year with more than 80% of cloud and shadow-free were acquired.

From 2006 to 2010, we also used coarse resolution SR data over the study area from the MODIS sensor on board the Aqua and Terra platforms. The MOD09CMG (called hereafter MOD09, lpdaac.usgs.gov/products/modis_products_table/mod09cmg) product provides SR images, in 7 channels from 450 nm to 2100 nm at a resampled spatial resolution of 0.05°, corresponding to the Climate Modeling Grid. We used collection 6 version. In the studied area, 0.05° is equal to approximately 5.5 km in latitude and 4 km in longitude. We also produced a nadir-corrected (zenith view angle is null, $\theta v = 0°$) product, called hereafter MODN, by applying the VJB model, a BRDF (Bidirectional Reflectance Distribution Function) correction method from Vermote et al. (2009). Solar zenith angles (θs) effects were not corrected, and we kept the value of the original MODIS data. MODIS acquisition, flagged in the MOD09 SR product with cloud and cloud/shadow cover, aerosol optical thickness higher than 0.6 or view zenith angle higher than 60°, were eliminated.

Existing LAI/FAPAR products, used for inter-comparison, were derived from the Aqua and Terra MODIS-15 LAI and FAPAR Collection 5 products (MCD15A3, lpdaac.usgs.gov/products/modis_products_table/mcd15a3, Myneni et al., 2002) and LAI and FAPAR GEOLAND-2 version 1 products (GEOv1, www.geoland2.eu/index.jsp, Baret et al., accepted for publication). MCD15A3 data are available at a 4-day time step based on a 4-day period at a 1 km resolution. MCD15A3 main algorithm is based on LUTs simulated with a three-dimensional RTM (Knyazikhin, Martonchik, Myneni, Diner, & Running, 1998). Red and NIR atmospherically corrected products (MOD09GA) and the corresponding illumination-view geometry are used as LUT inputs. The output is the mean LAI and FAPAR values computed over the set of acceptable LUT elements for which simulated and MODIS SR agree within a specific level of uncertainties. A back-up algorithm is used when the main algorithm fails. However, only the main algorithm retrieval is considered in this study. This product refers to LAI_{MOD15} and $FAPAR_{MOD15}$ in this paper. GEOv1 data are derived from the SPOT/VEGETATION SR data (1 km, daily), corrected from the view angle, at about 1 km resolution every 10 days using a 30-day temporal window. GEOv1 algorithm is based on a fusing approach between MODIS-15 and CYCLOPES products. CYCLOPES is a PROSAIL inversion algorithm using ANN, similar to the one applied on F2 and MODIS SR through this study. More description of the algorithm is provided in the next section. MODIS-15 and GEOv1 data were then averaged over the CMG (Climate Model Grid, 0.05°) based on the location of center of the 1 km pixel. Moreover, aggregated CMG pixels computed with a missing pixel were discarded.

3. Methodology

In this study, we used the BV-NNET (Biophysical Variables Neural NETwork) tool developed by Baret et al. (2007) to derive the global CYCLOPES LAI and FAPAR products. It is based on the calibration of Artificial Neural Networks learned on PROSAIL simulations. This method was applied to retrieve LAI and FAPAR from three input SR types: (i) F2 SR (to generate the reference maps), (ii) MODIS SR (estimates refer hereafter to NET_MOD09) and (iii) MODIS normalized SR at nadir (NET_MODN). The term NET_MOD refers to the two products. The inversion was performed at the native resolution for F2 SR data (i.e. 8 m), while the 0.05° CMG was used for MODIS SR data. F2 LAI and FAPAR were then aggregated at CMG resolution.

3.1. LAI and FAPAR estimation from BV-NNET

LAI and FAPAR were estimated from BV-NNET tool applied to F2 SR, and MOD09 and MODN SR from MODIS sensors on board of Aqua and Terra. It was necessary to build three single neural networks for the three SR sources because the number and nature of input data were not constant (depending on the spectral bands and the angular configurations). BV-NNET is divided in three core steps: learning database creation, neural network training, and trained neural network application.

The learning database used to train the Artificial Neural Networks (ANN) was made of bi-directional SR (ANN inputs) and corresponding LAI and FAPAR variables (ANN outputs). A wide range of cases were simulated using the PROSAIL radiative transfer model (Jacquemoud, Bacour, Poilve, & Frangi, 2000). PROSAIL results from the coupling between the PROSPECT leaf optical properties model (Jacquemoud & Baret, 1990) and the SAIL (Verhoef, 1984) models. PROSPECT was used to simulate leaf reflectance and transmittance (ρ_{leaf}, t_{leaf}) for a large range of leaf characteristics described by 5 parameters: the mesophyll structure parameter (N), chlorophyll (Cab), dry matter (Cdm), relative water (Cw) and brown pigment (Cbp) contents. Cab comprises chlorophylls a and b as well as carotenoids. Water content is linked to the dry-matter content in the form of green leaf relative water content which is assumed to vary within a relatively small range. Cbp corresponds to the brown pigments observed during leaf senescence. SAIL is used for the computation of the canopy bi-directional reflectance from ρ_{leaf}, t_{leaf}, the variables describing canopy structure (LAI, Average Leaf Angle — ALA and hot-spot parameter — HsD), fraction of pure vegetation (vCover, Baret et al., 2007), the angular characteristics s (solar zenith angle), v (view zenith angle), $\Delta\Phi$ (relative azimuth angle between view and solar angle) and the background reflectance

Table 1
Distribution characteristics of the input variables of the PROSAIL radiative transfer models used to generate the training database.

	Variable	Variable distribution					Co-distribution with LAI				Class
		Law	Min	Max	Mode	Std	Min (LAI = 0)	Max (LAI = 0)	Min (LAI = 8)	Max (LAI = 8)	
Canopy	LAI	Gaussian	0	8	2	2	–	–	–	–	6
	ALA (°)	Gaussian	30	80	60	20	30	80	55	65	4
	HsD	Gaussian	0.1	0.5	0.2	0.2	-	-	-	-	1
	vCover	Gaussian	0.05	1	1	0.2	0	1	1	1	2
Leaf	N	Gaussian	1.2	2.2	1.5	0.3	1.2	2.2	1.3	1.8	4
	Cab ($\mu g.m^{-2}$)	Gaussian	20	90	45	30	20	90	45	90	4
	Cdm ($g.m^{-2}$)	Gaussian	0.003	0.011	0.005	0.005	0.003	0.011	0.005	0.011	4
	Cw	Uniform	0.6	0.85	-	-	0.6	0.85	0.7	0.8	4
	Cbp	Gaussian	0	2	0	0.3	0	2	0	0.2	4
Soil	Bs	Log-Gaussian	0.16	1.3	0.586	0.14	0.5	3.5	0.5	1.2	4

spectrum. The latter is described by the spectral soil reflectances (ρ_{soil}) combined with a brightness coefficient (bs, Baret et al., 2007).

All of these variables, except ρ_{soil}, were randomly selected following pre-defined distributions (Table 1) and co-distributions with LAI. The type of distributions (uniform, Gaussian or log-Gaussian) and the associated parameters (minimum, maximum, mode and standard deviation) were equivalent to the original CYCLOPES parameterization (Baret et al., 2007). Similar parameterizations were also successfully applied on high resolution sensors by Bsaibes et al. (2009) with F2 data and Duveiller et al. (2011) with SPOT-HRV data. The sampling scheme is based on a full orthogonal experimental plan (Bacour, Jacquemoud, Tourbier, Dechambre, & Frangi, 2002) to account for all the interactions between variables, while keeping a range of variation for each variable densely and near randomly populated. Each distribution was thus divided into a number of classes which increases with the role of the variable in the radiative transfer process. The product of all classes determines the size of the LUT (i.e. 196,608 cases). Cases with unrealistic combinations between LAI and all other variables except HsD were excluded based on an empirically designed trapeze shape which delimited the valid interval of the co-distribution between LAI and the other variable. The trapeze is defined by four edges in the 2-dimensional LAI/other variable space: minimum and maximum of LAI and the other variable. Note that: (i) no view zenith and relative azimuth angles variation are used for NET_MODN simulations as SR were normalized to a constant nadir viewing angle; (ii) vCover is equal to 1 for F2 simulations as the pixel is considered as pure; (iii) the lower limit of ALA distribution was modified to 5° for F2 simulations to be consistent with in situ measurement of ALA from CAN-EYE software (not shown in this paper).

The spectral soil reflectances (ρ_{soil}) of a selection of 7 soil spectrums (Fig. 3) were extracted from the World Soil Database of the International Soil Reference Information Centre (ICRAF-ISRIC, 2010). The selected spectrums refer to spectrum sample in western European countries and are radiometrically close to bare soil reflectances observed in the study area with F2 bands (Claverie, 2012). The log-Gaussian distribution of the brightness coefficient (bs, see last row of Table 1) was adjusted in order to ensure a good matching between: (i) the range of bare soil spectrum observed with F2 bands and (ii) the range of bare soil spectrum simulated using the combination of the 7 previously selected spectrums and bs.

Conversely to LAI, FAPAR is not an input variable of PROSAIL. FAPAR was simulated for each case as the instantaneous black-sky value at 10:00 local solar time that corresponds to a good approximation of the daily integrated value under black-sky assumption (Baret et al., 2004).

Each neural network (one per ECV) consisted in a back-propagation network, following the configuration of CYCLOPES (Baret et al., 2007), with one sigmoid hidden layers and one output neuron. Nevertheless, the numbers of input data (N_{input}) were different from CYCLOPES, and between the three simulations:

(i) F2 includes 3 spectral bands (centered at 555, 650 and 830 nm) and 3 angular configuration parameters (θs, θv, ΔΦ). Due to residual errors after atmospheric correction, the blue band (488 nm) was not used as recommended by Baret et al. (2007) for SPOT-VGT or Bsaibes et al. (2009) for F2.
(ii) ECV_{NET_MODN} includes 4 spectral bands: 657, 863, 550, 1240 nm plus the solar zenith angle. Instead of using MODIS band 6 (1640 nm), similar to the SWIR band of SPOT-VGT (1640 nm) used in CYCLOPES, we used band 5 (1240 nm) which provided better results (results not shown for the sake of brevity). The blue band is not used for the same reasons as above.
(iii) ECV_{NET_MOD09} includes the same 4 spectral bands used for MODN, plus the 3 angular configuration parameters (θs, θv, ΔΦ).

As a result, the number of neurons of the hidden layer is slightly different. Mather and Koch (2010) have recommended using twice the number of neurons of the hidden layer as the number of the input

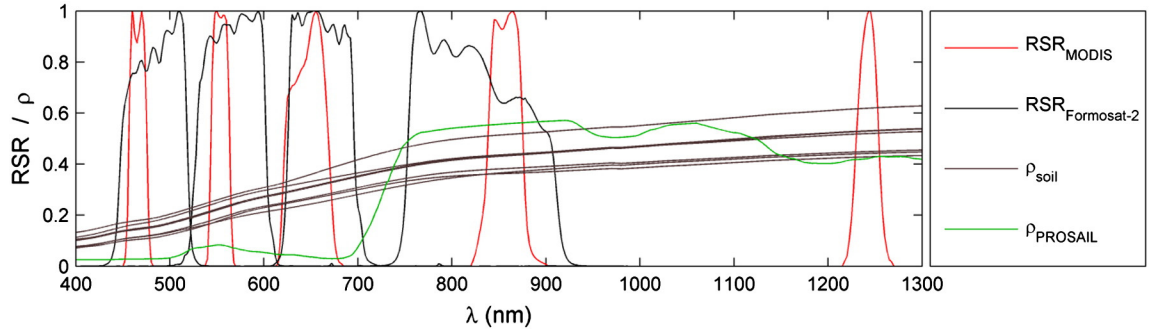

Fig. 3. Relative Spectral Response (RSR) of MODIS (red) and Formosat-2 (black) bands used in this study. The reflectance spectra of the 7 soil spectrums used (brown) and a typical canopy reflectance spectra simulated by PROSAIL (green) are also displayed. (For interpretation of the references to color in this figure legend, the reader is referred to the web version of this article.)

variables. However, as input spectral reflectances data are not totally uncorrelated, we found that increasing the number of neurons (e.g., up to $2 \times 7 = 14$ for ECV_{NET_MOD09}) did not improve performances. Consequently we applied a purely empirical rule by using $N_{input} + 1$ neurons in the hidden layer. The output layer included one linear neuron, as recommended by Weiss (1998) and Verger et al. (2011).

3.2. Direct comparison: spatial aggregation and temporal interpolation

Formosat-2 reference maps were validated through direct comparison with in situ measurements. LAI and FAPAR were extracted from the image using a 3×3 pixels window centered on the ESU. Solar and viewing geometry angles (θv, θs, and $\Delta\phi$) were calculated for the F2 image center. The mean and standard deviation were calculated from the 9 LAI/FAPAR F2 pixels. Despite the high frequency of satellite image acquisitions, the ground measurements did not necessarily coincide in time with the remote sensing observations. In situ measurements were interpolated at the dates of F2 using a cubic interpolation method which reflected a smooth and consistent temporal shape because of high measurements frequency. The interpolated values separated by more than 7 days of a measurement were excluded from the analysis.

CMG reference maps were computed through the aggregation of F2 reference maps. LAI and FAPAR 8-meter pixels, included in each CMG pixel, were averaged. A flag was added to exclude aggregated CMG pixel computed including cloud or cloud shadow contaminated F2 pixels.

Concerning the direct comparison against coarse resolution products, MOD15 (4-day, CMG) and GEOv1 (10-day, CMG) products were compared to F2 data included in the 4-day and 10-day periods, respectively. Only coincident (same day) data between F2 and ECV_{NET_MOD09} and ECV_{NET_MODN} products (1-day) were maintained for the analysis.

3.3. Statistical metrics

At each stage of the validation, four statistical metrics were used to quantify the deviation between two datasets:

- the Accuracy (A) and the relative Accuracy (rA),

$$A = \frac{1}{N} \times \sum_{i=1}^{N} \varepsilon_i \quad ; \quad rA = 100 \times \frac{A}{\overline{M}} \tag{1}$$

- the Precision (P) and the relative Precision (rP),

$$P = \sqrt{\frac{1}{N-1} \times \sum_{i=1}^{N} (\varepsilon_i - A)^2} \quad ; \quad rP = 100 \times \frac{P}{\overline{M}} \tag{2}$$

- the Uncertainty (U) and the relative Uncertainty (rU),

$$U = \sqrt{\frac{1}{N} \times \sum_{i=1}^{N} {\varepsilon_i}^2} \quad ; \quad rU = 100 \times \frac{U}{\overline{M}} \tag{3}$$

- the correlation coefficient,

$$r^2 = \left[\frac{\mathrm{cov}(x,y)}{std(x) \times std(y)}\right]^2 \tag{4}$$

where N is the number of valid samples used for the comparison, ε_i is the difference between two simultaneous data x_i and y_i that are compared and $\overline{M}$ is the mean value of the reference observation. *cov* and *std* relate to the covariance and the standard deviation, respectively. The three first metrics were used to quantify the mean bias (A), the repeatability (P) and the actual statistical deviation (U, also called RMSD) of the estimates (Vermote & Kotchenova, 2008).

To quantify the smoothness of the products through time, we computed an estimate of the time series noise based on the method developed by Vermote et al. (2009, Eq. (4)). Given three successive measurements, a triplet i, i + 1, and i + 2, the statistical difference between the center measurement and the linear interpolation between the two extremes quantifies the "noise" of *y* variable. This estimate assumes thus a local linear variation between three dates, which can be regarded as true throughout the time series except for sharp transitions. Relative noise (Eq. (6)) was computed by dividing the noise by the mean of the time series ($\overline{M}$) to facilitate comparison across SR, LAI and FAPAR. We considered a maximum period of 20 days between day_i and day_{i+2}, corresponding to 3 consecutive GEOv1 data.

$$Noise(y) = \sqrt{\frac{\sum_{i=1}^{N-2} \left(y_{i+1} \times \frac{y_{i+2} - y_i}{day_{i+2} - day_i} \times (day_{i+1} - day_i) - y_i \right)^2}{N-2}} \tag{5}$$

$$RelativeNoise(y) = 100 \times \frac{Noise(y)}{\overline{M}} \tag{6}$$

4. Results

4.1. Evaluation of the surface reflectance

To ensure proper comparison of ECV products, we first verified that MODIS Terra or Aqua and F2 surface reflectances (SR) are consistent at CMG spatial resolution. Fig. 4a–h shows the direct comparison of SR derived from F2 (aggregated over CMG) and MODIS on board the Terra satellite (analysis with data from Aqua satellite leads to similar results) acquired on simultaneous days. Overpass time of MODIS Terra and F2 are around 10:30 and 09:30 local solar time at the equator, respectively. In Fig. 4a–d, MODIS SR are compared directly without any BRDF corrections (original MODIS geometric conditions referring to θ_{MODIS}), while in Fig. 4e–h, they were normalized at F2 geometric conditions (referring to θ_{F2} and including both F2 view and solar angles) using the VJB model. Without considering BRDF correction, the scattering between both sensors is significant, especially in the visible bands (r^2 are 0.33, 0.22 and 0.29 for red, green and blue bands, respectively). The two dark stripes (red and green bands mainly) correspond to two main angular configurations of MODIS sensor. The scattering is significantly reduced after BRDF correction (precisions are 3 times lower except for the blue band). This agreement shows the good performance of: (i) both instruments radiometric calibration, (ii) the VJB model and (iii) the two atmospheric correction methods applied to F2 data (Hagolle et al., 2008) and to MODIS data (Vermote & Kotchenova, 2008; Vermote, El Saleous, & Justice, 2002) for green, red and NIR bands. The blue band displays lower correlation (0.54), due mainly to a high influence of aerosol content in these wavelengths. Nevertheless, biases remain between the two SR factors: $+3.10^{-2}$ for NIR, -3.10^{-3} for red and $+3.10^{-3}$ for green. These residual biases are due to significant differences in term of sensor spectral response (Fig. 3). Indeed, they are consistent with the biases deducted from the comparison of synthetic SR factors simulated with PROSAIL model (Fig. 4j–m). By applying the linear fits of Fig. 4j–m as a band-pass correction to the MODIS data of Fig. 4e–h, the absolute biases are reduced to less than 1.10^{-3} for red and green bands and 2.10^{-3} for NIR band (results not shown for the sake of brevity).

The same analysis was performed using statistical metrics computed per bins as suggested by Vermote and Kotchenova (2008). Fig. 5 displays the repartition of the statistical metrics through the variation of F2 SR compared to suggested specification for MODIS SR introduced by these authors ($0.005 + 0.05\rho$). After BRDF correction (Fig. 5e–h),

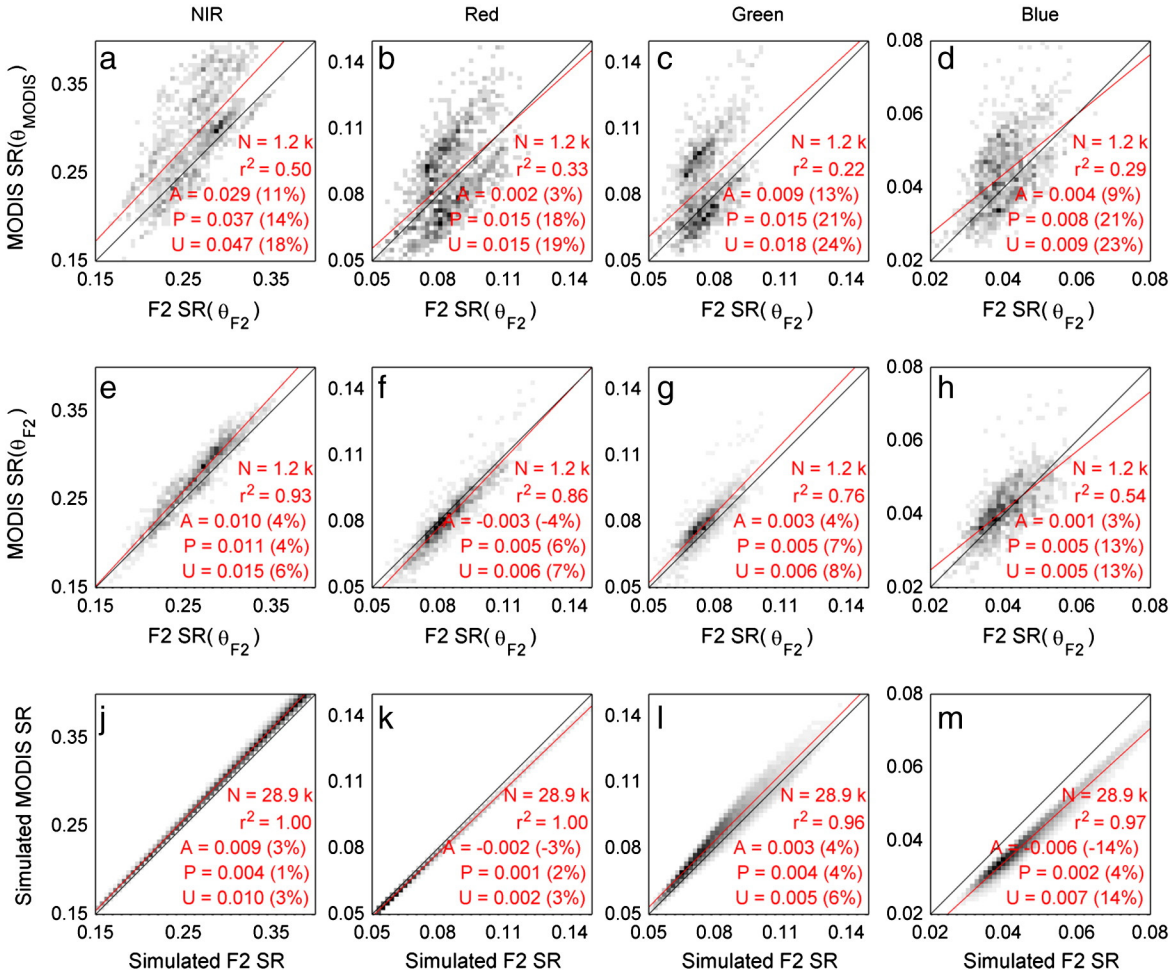

Fig. 4. Comparison of aggregated Formosat-2 (F2) and MODIS Terra Surface Reflectances (SR) with (subplots e–h) and without (subplots a-d) BRDF-correction. BRDF corrections were performed with the VJB model method using for each individual MODIS acquisition, the angular configuration (denoted as θ_{F2}) of Formosat-2 data acquired the same day. Subplots j-m show the comparison of synthetic F2 and MODIS SR simulated with PROSAIL model. The simulated dataset is the same as the one described in Section 3.1. The limits of the axis are cropped to the same limits as subplots a–f. Plots are represented through density function from light gray (minimum) to black (maximum); white means no data. Red lines correspond to the linear fits. r^2, A, P and U refer to the statistical metrics given in Section 3.3. Relatives A, P and U are reported under bracket. N is the number of points. (For interpretation of the references to color in this figure legend, the reader is referred to the web version of this article.)

the metrics stay under the specifications except for some extreme values. The variations of the metrics of Fig. 5e–h along the F2 SR bins are weak compared to those of Fig. 5a–b. They are consistent with the metrics computed on simulated data (Fig. 5j–i) except for the precisions which are bigger, as expected since observed data are compared with simulated data.

4.2. Validation of Formosat-2 reference maps

The retrieved biophysical variables are presented in Fig. 6 against a total of 40 interpolated in situ measurements over 7 ESU sites. The F2 estimates of the two biophysical variables are in good agreement with the ground measurements since it yields to an overall uncertainty of 0.35 for LAI, and 0.07 for FAPAR. Positive LAI biases (+0.07) reflect a small overestimate, mainly for the highest value observed on soybean, while small negative biases were associated with FAPAR estimations (−0.04). Inter-crop disparities are, nonetheless, significant. Best performances are retrieved with maize and soybean (Uncertainty = 0.24–0.37). Greatest errors are retrieved for sunflower (LAI and FAPAR Uncertainty: 0.5 and 0.12) which displayed the biggest heterogeneity (see vertical standard deviation bars), known as a significant source of error of DHP in situ measurements (Demarez et al., 2008; Jonckheere et al., 2004). This level of error remains in agreement with previous studies based on the same tool (Bsaibes et al., 2009; Duveiller et al., 2011; Verger et al., 2011). 90% of LAI estimates and 78% of FAPAR estimates fit within the required range of accuracy identified by GCOS (2011). Overall accuracies remain acceptable except for sunflower FAPAR.

4.3. Aqua and Terra ECV estimates comparison

Fig. 7 shows the comparison between Terra and Aqua daily ECV estimates derived from both MOD09 and MODN SR. Both estimations are highly correlated ($r^2 > 0.93$), U remains small (~0.12 for LAI and ~0.027 for FAPAR) and Accuracy are almost null. The use of MODN instead of MOD09 SR as inputs improves the consistency of LAI estimates below 0.5. Higher LAI values are very similar. Considering the important observational geometry differences between Terra and Aqua acquisition, these results highlight the impact of the BRDF correction VJB model (Fig. 7c, d) and the PROSAIL model (Fig. 7a, b). Moreover, the use of the solar zenith angle as a BV-NNET input limits residual effects on ECV value from solar geometry differences between the two sensors. Due to the overall agreement between Aqua and Terra estimates, we decided to merge the 2 estimates by producing daily averaged LAI and FAPAR, corresponding to the average of Aqua and Terra estimates or only one of them when both were not available (due mainly to cloud cover).

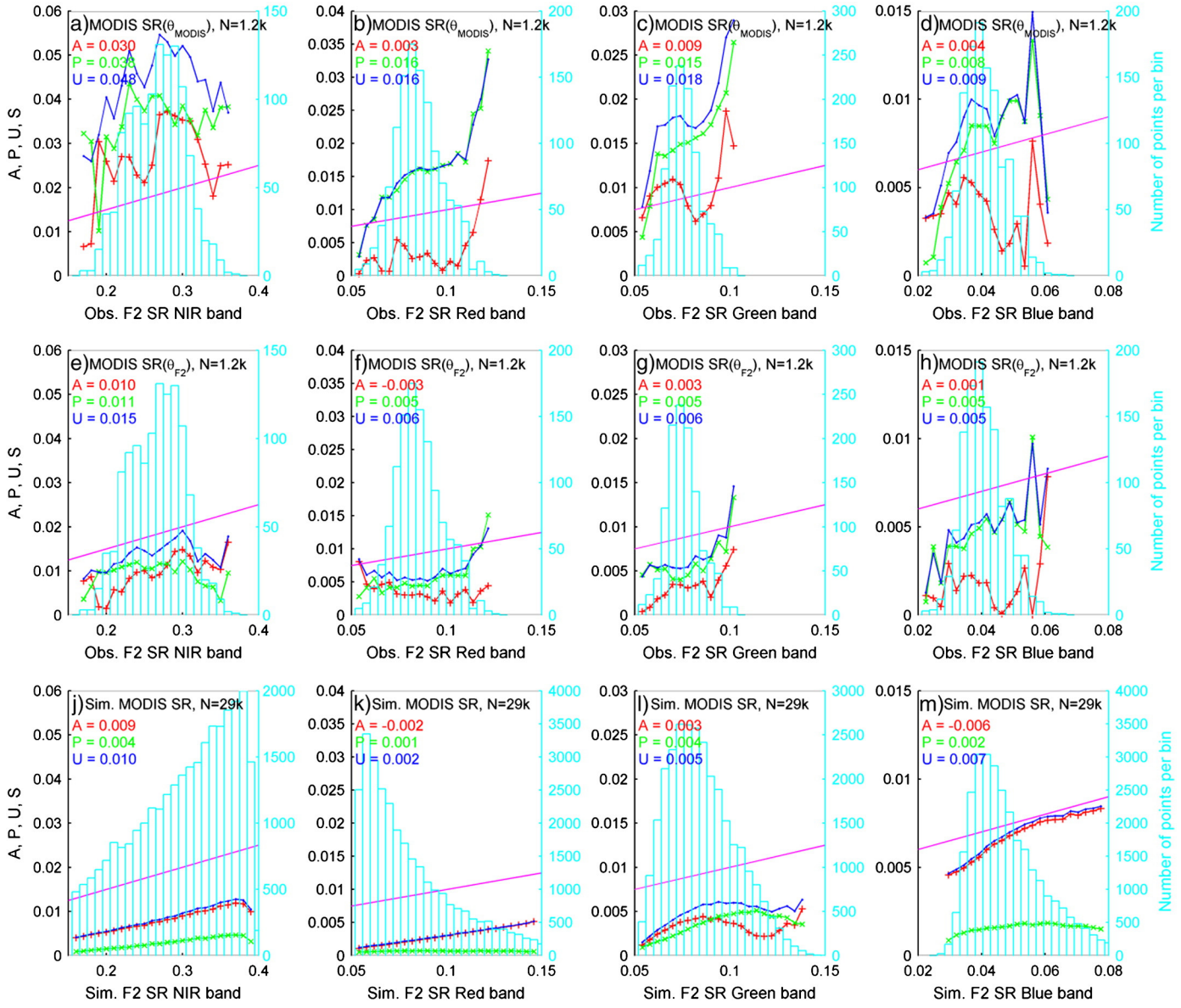

Fig. 5. Accuracy (A, red), Precision (P, green) and Uncertainty (U, blue) of the MODIS Terra SR with (subplots e–h) and without (subplots a-d) BRDF-correction over 25 F2 aggregated SR bins. Notice that A corresponds to the absolute value of the accuracy described in Eq. (1). Also shown are the number of points per bin (cyan bars) with the value on the left and the error budget of suggested uncertainties (magenta line). (For interpretation of the references to color in this figure legend, the reader is referred to the web version of this article.)

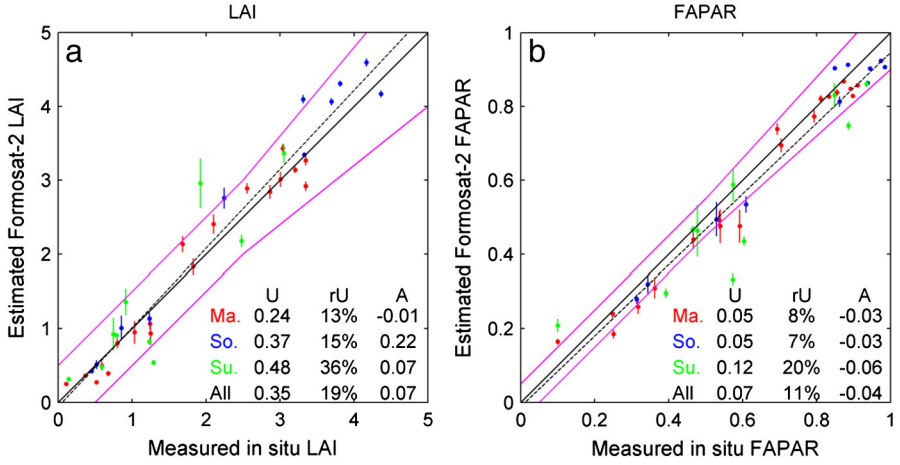

Fig. 6. LAI (a) and FAPAR (b) reference maps validation scatterplots. In situ measurements are derived from DHPs acquired on ESUs over maize (Ma, red), soybean (So, blue) and sunflower (Su, green) fields. Estimates (mean — dots- and ± standard deviation — vertical bars) are derived from a 3 × 3 pixel window of Formosat-2 data. Black dashed line represents the overall fit and magenta lines the GCOS specifications boundaries (max(0.5, 20%) for LAI and max(0.05, 10%) for FAPAR).

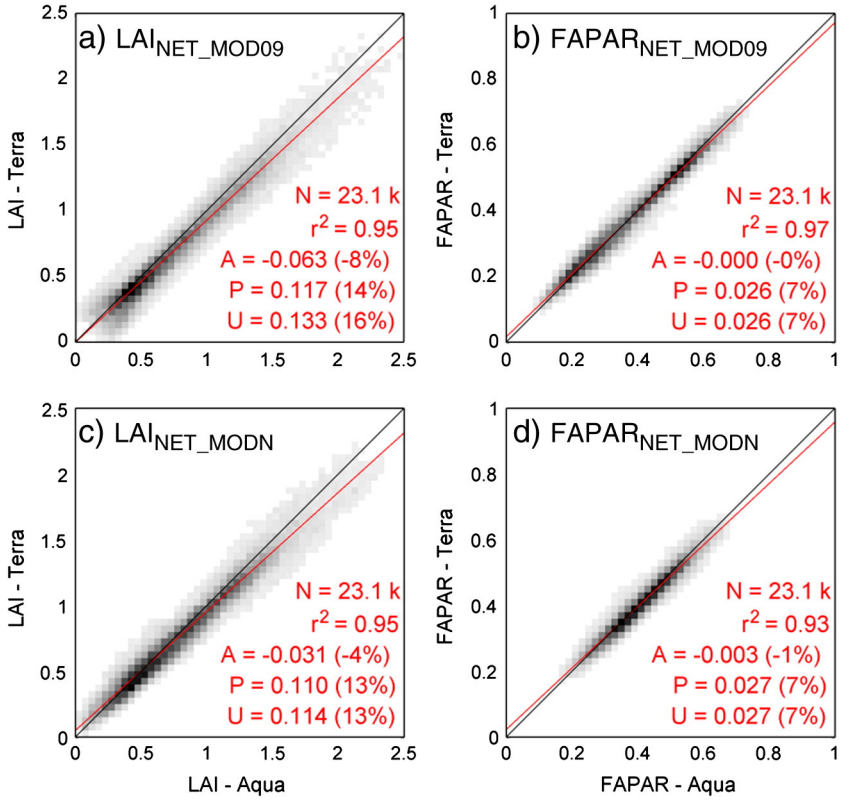

Fig. 7. LAI and FAPAR comparison of estimates derived from Aqua and Terra surface reflectances corrected (NET_MODN, subplots c-d) or not (NET_MOD09, subplots a–b) from BRDF effects. Refer to Fig. 4 legend.

4.4. Evaluation against ECV reference maps

The direct comparisons between coarse resolution reference maps and ECV products are shown in Fig. 8 for LAI and Fig. 9 for FAPAR. Concerning LAI, the best estimation is observed with NET_MODN products and all retrievals fit the GCOS uncertainty requirement (±0.5). Low LAI are unbiased whereas values greater than 1.5 are slightly overestimated. Estimation of LAI_{NET_MOD09} shows a higher precision (0.15) with a negative accuracy of −0.07 and an uncertainty of 0.17. In Fig. 8e, 70% of the errors are mainly negative. However, greatest values (LAI > 1.5) are slightly overestimated. The rU calculated for LAI_{MOD15} (23%) is above the reference map rU but 98% of the retrievals fit the

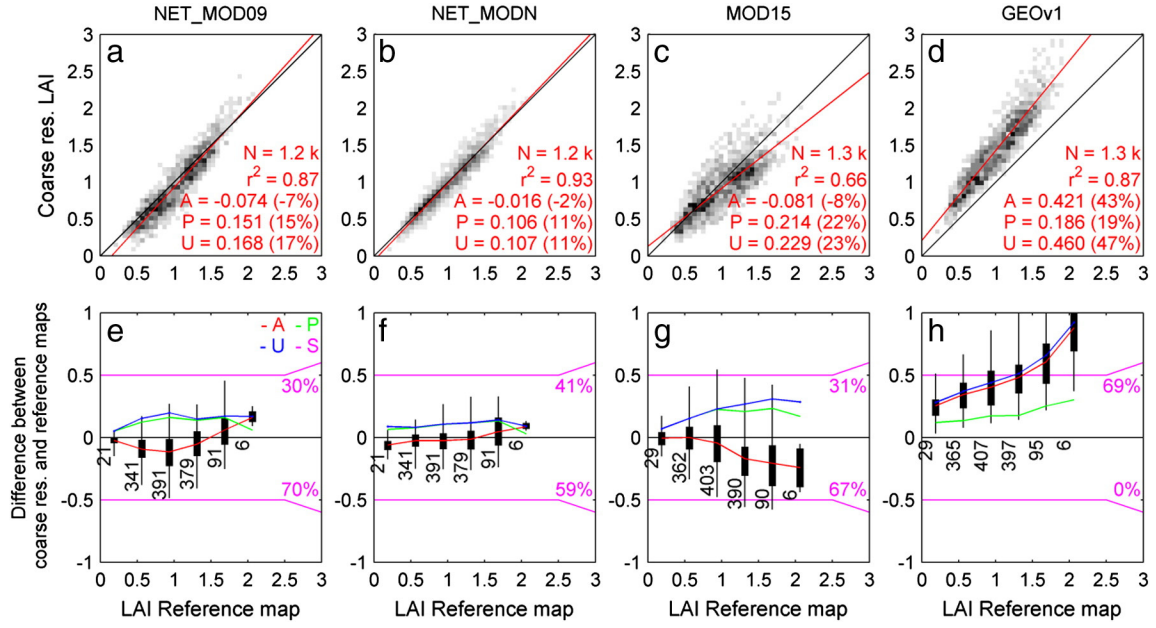

Fig. 8. LAI coarse resolution validation. Subplots a–d: direct comparison between LAI coarse resolution (y-axis) and LAI reference map (x-axis). Refer to Fig. 4 legend. Subplots e–h: absolute difference between coarse resolution and reference map LAI displayed through boxplot: 1st and 99th percentiles (line), 1st and 3rd quartiles (black box). The Accuracy (A, red), the Precision (P, green) and the Uncertainty (U, blue) are computed per bins. The number of data included in each of the 0.3 bins is shown in the bottom of the boxplot. The magenta lines correspond to ±max(0.5, 20%) GCOS (2011) specifications (S) boundaries and magenta percentages correspond to the amount of data included in 2 sections delimited by −max(0.5, 20%), 0 and +max(0.5, 20%). (For interpretation of the references to color in this figure legend, the reader is referred to the web version of this article.)

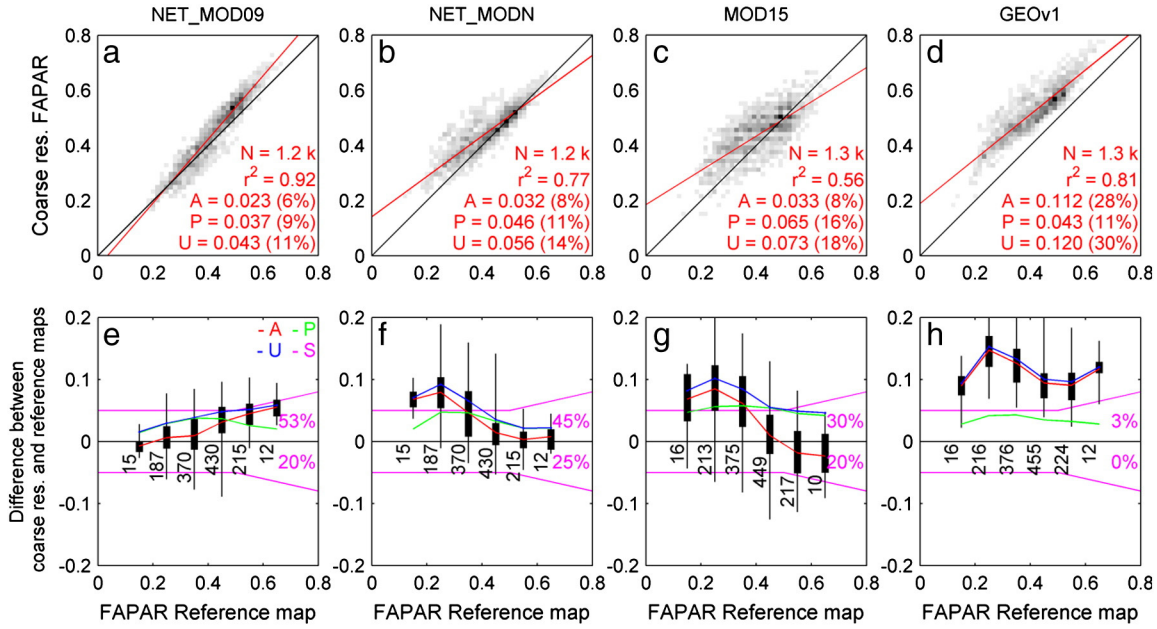

Fig. 9. Idem Fig. 8 but for FAPAR coarse resolution validation. Magenta lines on e–h correspond to the GCOS (2011) specifications boundaries (±max(0.05, 10%)).

GCOS specification (S). Data are less correlated than the two other products and the underestimation is strong, mainly for values greater than 1. This underestimation is in agreement with the conclusion of Garrigues et al. (2008) who have found a small underestimation of LAI_{MOD15} compared to two effective LAI measurements on a crop site. The underestimation is also visible in the study of Fang, Wei, and Liang (2012) where comparisons have been based on true LAI. However, in this study, we considered effective LAI measurements which may be lower than MOD15 LAI defined as true LAI for non-regular clumped canopies (Weiss et al., 2004). This result demonstrates the difficulty to accurately quantify the clumping factor as observed by Demarez et al. (2008) for cropland canopies. The Uncertainty of 0.23 from Fig. 8c remains nonetheless lower than the ones deducted over cropland/grassland biomes from these previously mentioned studies (Fang et al., 2012; Garrigues et al., 2008) mainly because the scale of the analysis is coarser. LAI_{GEOv1} displays a good precision (19%) but related to a strong positive Accuracy (43%). In the observed range of values (LAI < 3), GEOv1 estimates over croplands are mainly derived from CYCLOPES estimates (refer to the weighted function described in Baret et al., accepted for publication) whose algorithm is equivalent to BV-NNET. The precision (better than LAI_{MOD15} precision) shows thus the consistency of the algorithm. However, the bias points out discrepancies between the two inputs SR data: F2 for reference maps and SPOT/VEGETATION for GEOv1. Moreover, the analysis showed previously a small underestimation of MOD15 LAI.

Concerning FAPAR (Fig. 9), the $FAPAR_{NET\_MOD09}$ product performs better than $FAPAR_{NET\_MODN}$ one against reference maps. Indeed, $FAPAR_{NET\_MOD09}$ product displays the highest correlation and the lowest error (Uncertainty = 0.04) and 73% of the retrieval remains under the stringent max(0.05, 10%) limits required by GCOS. The slope of the regression slightly differs from the 1:1 line due to overestimation of high FAPAR. The $FAPAR_{NET\_MODN}$ is overestimated, mainly for the low values (<0.4) and the relative differences (14%) exceeds the reference map uncertainty (11.3%). NET_MODN and NET_MOD09 yield to low differences on LAI retrievals and significance differences on FAPAR retrievals. Not shown in this paper, one third of the simulated LUT was used to validate the network generated using the two other thirds. The analysis of this theoretical validation shows that NET_MOD09 network performance is 11% better than NET_MODN network performance for FAPAR and only 4% better for LAI. Concerning $FAPAR_{MOD15}$, the low values are overestimated while the accuracy is low for the highest values. $FAPAR_{MOD15}$ displayed a significant scattering ($r^2 = 0.56$). One of the explication of the divergence is the definition itself of the FAPAR which is computed for the satellite overpass solar time for MOD15 (about 10:30 and 13:30 at the equator) while BV-NNET FAPAR are computed for a constant solar time (10:00), considered as a good estimate of the daily integrated FAPAR (Baret et al., 2004). Finally, the overestimation of $FAPAR_{GEOv1}$ is similar to the one observed for LAI.

4.5. Time series analysis

In addition to the previously presented quantitative validation, Fig. 10 shows the LAI and FAPAR temporal profiles of the different products for 3 selected pixels (see A, B and C letters to locate the pixels in the map of Fig. 2). All products consistently reproduce the overall crop phenology. The green-up periods are systematically fast whereas the senescence rate varies from year to year. The presence of 2 peaks (e.g., pixel A) is related to an equivalent proportion in CMG pixel of winter crops (wheat and rapeseed, 25%) and summer crops (maize, sunflower and soybean, 30%) which phenologies are delayed. However, notice that due to the 30-day window used in the LAI_{GEOv1} compositing, the two peaks of pixel A are less pronounced than for other products. LAI and FAPAR peaks dates range systematically between mid and end of May. This corresponds to the end of the full vegetated winter crops fields and the beginning of the summer crop growing season. Finally, peaks observed on the 4 coarse resolution products are correctly synchronized without lag.

Fig. 10g–h highlights the difference in magnitude between coarse resolution products and reference maps. LAI_{GEOv1} displays a systematic overestimation throughout the year included from 0.1 to 1, which is consistent with previous results. LAI_{NET_MODN} and LAI_{NET_MOD09} present similar magnitude of the reference maps peaks: differences do not exceed 0.25 (Fig. 10g). The annual LAI_{MOD15} peaks are systematically underestimated compared to the other products. This reflects the underestimation of cropland LAI_{MOD15} products compared to LAI CYCLOPE products identified by Camacho et al. (accepted for publication). These authors observed this underestimation mainly over “broadleaf crops” land cover which represents 90% of our study area. The winter LAI of the 3 coarse resolution products are in agreement with the reference maps: yearly minimum LAI is between 0.4 and 0.6. It never reaches 0 since CMG pixels generally comprise a small fraction of evergreen grassland and natural vegetation. We also observe differences for FAPAR. Winter $FAPAR_{NET\_MODN}$ (minimum between 0.2 and 0.4) is consistent

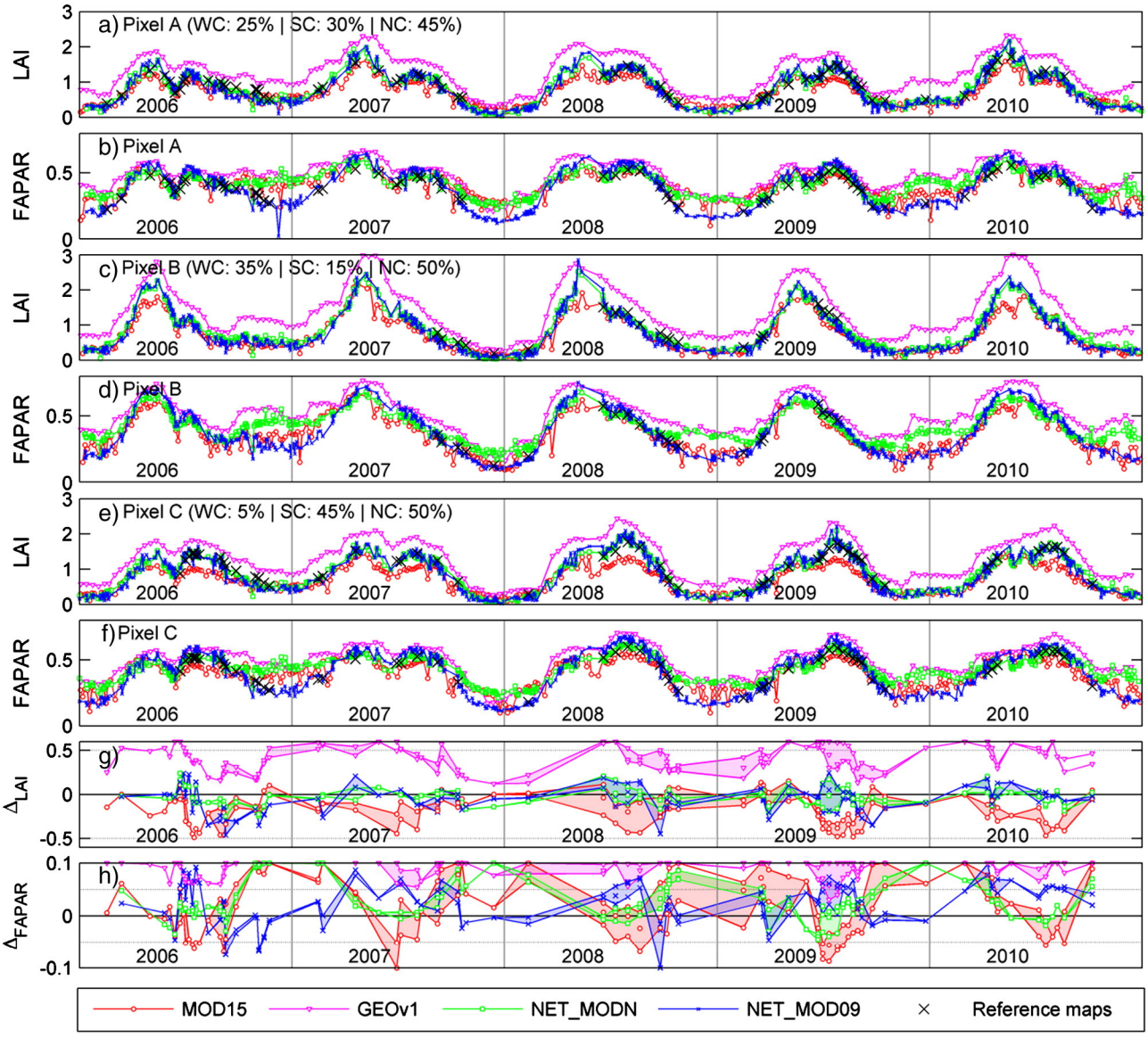

Fig. 10. Five-year coarse resolution LAI (subplots a, c, and e) and FAPAR (subplots b, d, and f) time series of 3 selected pixels (A, B and C, see locations in Fig. 2). Pixel A includes an equivalent proportion of Winter Crops (WC) and Summer Crops (SC); pixels B and C include a bigger proportion of winter and summer crops, respectively. WC, SC and Non-Crop (NC) proportions are given in subplots a, c and e. Absolute differences between coarse resolution estimates and reference maps (Δ_{LAI} and Δ_{FAPAR}) for the 3 pixels are displayed in subplots g and h. The Δ envelope is colored using same color as the legend. Δ higher than ±0.6 and ±0.1, for LAI and FAPAR respectively, were set to ±0.6 and ±0.1. No reference map data were acquired in 2006 and 2010 for pixel B as it is located on the side of the footprint. Vertical gray bars represent 1st day of year. (For interpretation of the references to color in this figure legend, the reader is referred to the web version of this article.)

with $FAPAR_{GEOv1}$ (0.2–0.5) but not with $FAPAR_{NET\_MOD09}$ (0.05–0.2). Winter $FAPAR_{MOD15}$ are more contrasted and display better agreement with $FAPAR_{NET\_MODN}$/$FAPAR_{GEOv1}$ on pixels A and C and with $FAPAR_{NET\_MOD09}$/reference maps on pixel B. Due to winter cloud cover and weak interest of this period for crop monitoring, only few reference maps were available. Nonetheless they emphasize that winter $FAPAR_{NET\_MOD09}$ best agrees with FAPAR reference maps. These differences are discussed in more detail in Section 4.6.

Products display relatively smooth time series. However, few outliers (sharp peaks) are observed on both NET_MOD products which may be due to cloud masking omission (e.g., October 2006). Note that the impact of misclassified cloud pixel is higher on FAPAR than on LAI. Although MOD15 is a composited product, we observe a larger number of outliers. To quantify the smoothness of the product, we computed an estimate of the time series noise based on the method previously described in Section 3.3.

Relative noises computed for the 4 coarse resolution products and the reference map are indicated in Table 2, including SR and ECV noises. Only 19 triplets per pixels were available for the reference map to compute noises, providing a noise on SR reference map of 2.7% in average. This result demonstrates the quality of the cloud detection and atmospheric correction performed by Hagolle et al. (2008, 2010). Note however that the view direction of F2 was almost constant during the 5 years, limiting the BRDF effects that impact the computed noise. The LAI noise is higher than SR ones, but remains very low. The biggest noise reduction from SR noise to ECV noise is observed for MOD09 time series (SR noises range from 18.7% to 29.9% depending on the band while ECV noises are 10.1% and 17.9%). SR_{MOD09} are, indeed, not corrected from surface anisotropy. This noise reduction demonstrates the impact of PROSAIL BRDF simulations. The noise observed for MODN SR is significantly lower than that of MOD09 SR, as expected since data were normalized from viewing angle. SR_{MOD0N} noises remain

Table 2
Relative noise calculated on Surface Reflectance (SR, column 3) and ECV (column 4) time series of the 4 datasets under study. Column 1 indicates the 5-year average number of triplets (i − 1, i, i + 1) of the SR and ECV time series per CMG pixel, where $day_{i+1} - day_{i-1} \leq 20$.

	Average triplet number	SR noise	ECV noise
Reference map	19	Green band: 2.5% Red band: 3.8% NIR band: 1.7%	LAI_{F2}: 4.0% $FAPAR_{F2}$: 2.5%
MOD09	547	Red band: 28.8% NIR band: 18.4% Green band: 29.9% MIR band: 18.7%	LAI_{NET_MOD09}: 17.9% $FAPAR_{NET\_MOD09}$: 10.1%
MODN	548	Red band: 13.6% NIR band: 5.0% Green band: 20.1% 1240 nm band: 4.9%	LAI_{NET_MODN}: 10.1% $FAPAR_{NET\_MODN}$: 6.4%
MOD15	370	–	LAI_{MOD15}: 16.4% $FAPAR_{MOD15}$: 13.9%
GEOv1	104	–	LAI_{GEOv1}: 2.3% $FAPAR_{GEOv1}$: 1.7%

in a similar range as Vermote et al. (2009). ECV_{NET_MODN} noises are included in the range of SR_{MOD09} noises and remain lower than ECV_{NET_MOD09} noises. Concerning the noise calculated on MOD15 and GEOv1 products, the temporal resolution and compositing reduced the noise level (day_{i+2}–$day_i \geq 8$ and 20 for MOD15 and GEOv1, respectively) as compared to the daily ECV_{NET_MOD} products (day_{i+2}–$day_i \geq 2$). Based on an average of 370 triplets per pixel, the ECV_{MOD15} noises (16.4% and 13.9%) are higher than ECV_{NET_MOD} except LAI_{NET_MOD09}. GEOv1 noises (1.7% and 2.3%) illustrate the smoothness of GEOv1 products mainly due to the 30-day window used for compositing (Baret et al., accepted for publication).

4.6. Product inter-comparison

Fig. 11 displays the 5-year pixel to pixel comparison of NET_MOD09, NET_MODN, MOD15 and GEOv1 LAI (Fig. 11a–f) and FAPAR (Fig. 11g–l) products estimated for the same day for NET_MOD products and during the 4-day and 10-day periods for MOD15 and GEOv1. Based on a very large number of samples, products are globally in good agreement with significant positive correlation. LAI_{GEOv1} are highly correlated with NET_MOD products ($r^2 > 0.9$) with a persistent accuracy relating the higher LAI_{GEOv1} values. This overestimation of LAI_{GEOv1} over cropland biome has recently been shown by Fang et al. (2013). LAI_{MOD15} displays largest scatterings with the 3 other LAI estimates (Fig. 11b–d). The r^2 between LAI_{NET_MOD09} and LAI_{NET_MODN} products (0.95) is greater than the one calculated between normalized and not normalized SR (not shown in this paper; red: 0.75; NIR: 0.85). This agreement demonstrates the acceptable consistency of the two BRDF assumptions (PROSAIL model for LAI_{NET_MOD09} and VJB model for LAI_{NET_MODN}) apply on MODIS CMG SR acquired over cropland. As introduced in Section 4.5, the bias and deviation between $FAPAR_{NET\_MOD09}$ and $FAPAR_{NET\_MODN}$

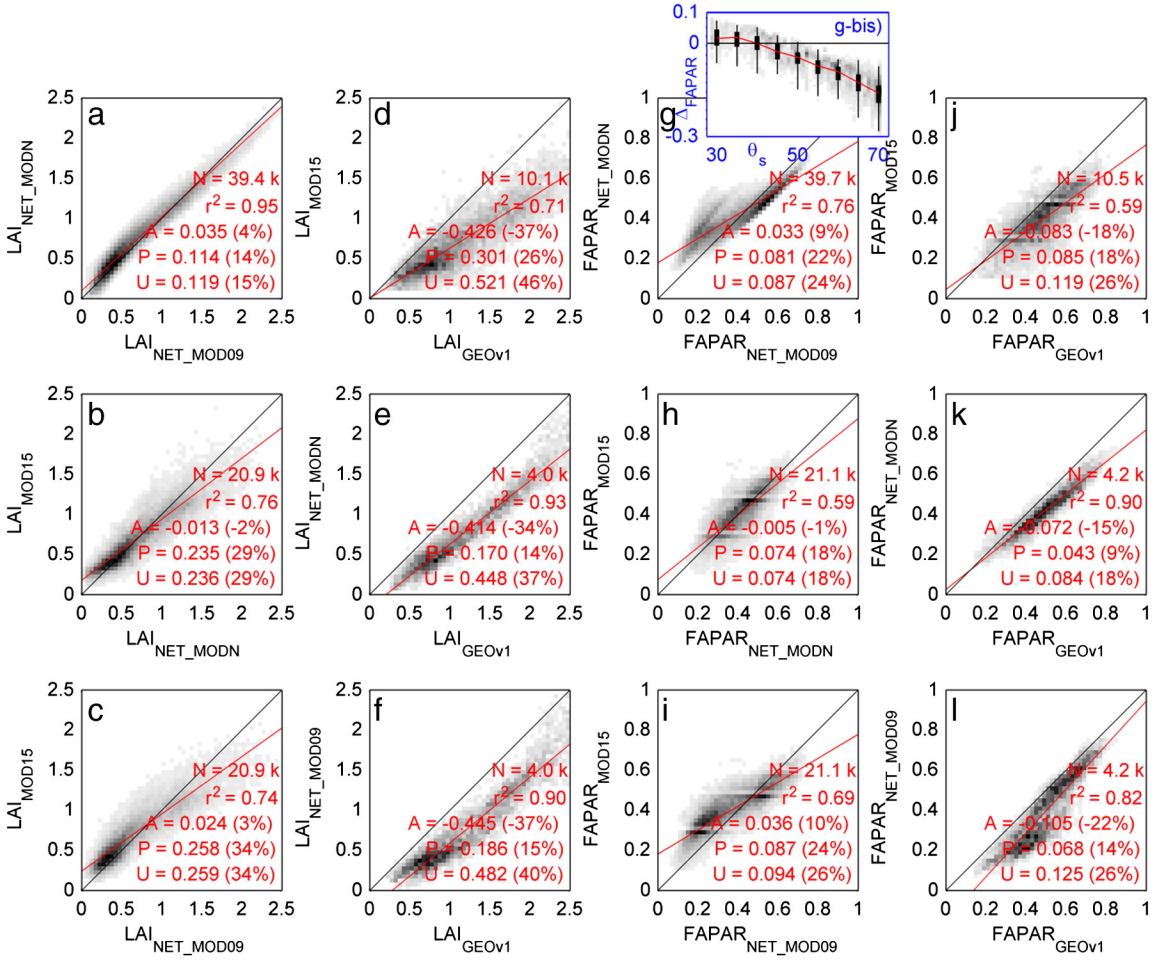

Fig. 11. Direct comparison between coarse resolution products (MOD15, NET_MOD09, and NET_MODN) for LAI (subplots a–f) and FAPAR (subplots g–l). To compare MOD15 and GEOv1 products to the two daily NET_MOD products, we averaged valid NET_MOD data acquired during the 4-day and 30-day periods of the composite. Subplot g-bis shows the comparison between s and Δ_{FAPAR} ($FAPAR_{NET\_MOD09} - FAPAR_{NET\_MODN}$). Boxplots show the distributions for each 5° increment of s and the red line connects the medians. Refer to Fig. 4 legend. (For interpretation of the references to color in this figure legend, the reader is referred to the web version of this article.)

are high for low values (Fig. 11g). These values are observed mostly during winter season when bare soil has the biggest impact on the signal. Conversely to the VJB model where the BRDF pattern is driven by the NDVI value (including thus low bare soil NDVI), PROSAIL model does not include soils BRDF as soils are assumed to be Lambertian. Winter season is also related to highest θ_s, which magnifies the anisotropy effects and thus the deviation between the two products (Fig. 11g-bis). Low $FAPAR_{GEOv1}$ products are more consistent with low $FAPAR_{NET\_MODN}$ products since both SR input data are BRDF-corrected before the application of BV-NET. In the same way as for LAI, $FAPAR_{MOD15}$ displays the lowest correlation with the 3 other products ($r^2 < 0.69$). MOD15 products are derived from a hybrid method concerning soil anisotropy effects assumption: over cropland area, soil is assumed Lambertian while a soil BRDF model is used over none-cropland area (Knyazikhin et al., 1999). The land cover heterogeneity at CMG level composed of a majority of cropland and some shrubland, forest and urban pixels may impact on the observed scattering but does not allow a firm conclusion concerning observed $FAPAR_{MOD15}$ differences.

4.7. ECV evaluation at finer spatial resolution

The whole analysis of this study was completed at the CMG spatial resolution (0.05° in geographic coordinates) since this resolution limits geometric scan effects which occur on the side of the images and the Point Spread Function (PSF). However, the averaging reduces the spatial variability. AS GCOS (2011) recommends delivering LAI/FAPAR estimates at 250 m, it is required to confront the algorithm with finer spatial resolutions. Fig. 12 displays the direct comparison of reference maps ECV and ECV_{NET_MOD09} derived from none BRDF-corrected 500 m SR data (250 m MODIS SR are not provided for green and 1240 nm bands) and aggregated SR data (1 km to 4 km). The figure highlights the decrease of the precision (and thus the uncertainty) with the increase of the resolution due to the limitation of geometric effects (scan effects, PSF, co-registration error). Notice that the relative accuracies are preserved along the resolution and are consistent with the relative accuracies computed at CMG level (Figs. 8a and 9a). At 500 m, 84% of LAI_{NET_MOD09} meets the GCOS requirement (max(0.5, 20%)) compared to 98% at 4 km. Concerning FAPAR, GCOS requirement are more difficult to achieve since only 49% at 500 m and 74% at 4 km are below max(0.05, 10%).

5. Conclusion

In this study, the performances of four LAI/FAPAR satellite products were evaluated over cropland using a coarse spatial sampling of 0.05° and a very high temporal sampling. We focused on one of the recently released official LAI/FAPAR MODIS products (MCD15A3, 1 km, 4-days), the European GEOLAND-2 LAI/FAPAR products (GEOv1, Baret et al., accepted for publication) and two LAI/FAPAR products derived from the BV-NNET tool (Baret et al., 2007) applied on MODIS surface reflectance (MOD09CMG, 0.05°, daily) BRDF-corrected (NET_MODN) and non-BRDF-corrected (NET_MOD09). The evaluation was based on quantitative and qualitative assessments of the deviation between the four products and LAI and FAPAR reference maps. The latter were derived from BV-NNET tool applied on 105 high spatial and temporal resolution sensor Formosat-2 (8 m) images acquired from 2006 to 2010 over a cropland site in Southwest France. The maps were first validated at a local scale using an intensive LAI/FAPAR in situ measurements campaign, and then aggregated at a coarse spatial resolution (0.05°).

At a local scale, BV-NNET tool applied on Formosat-2 data demonstrated a high level of robustness over the study area, i.e. croplands. It resulted to uncertainties of 0.35 and 0.07 for LAI and FAPAR, respectively, when compared with in situ measurements acquired over three crop types.

Inter-comparison of MODIS and aggregated Formosat-2 surface reflectances (SR) highlighted the good quality of two distinct atmospheric correction methods (Hagolle et al., 2008; Vermote et al., 2002) applied on two very different satellite data sets and of the BRDF correction VJB model (Bréon & Vermote, 2012; Vermote et al., 2009) applied to MODIS data. The deviations between Formosat-2 and MODIS SR estimates were reduced by a factor of approximately 4 after angular effects correction.

This study provided one of the first intensive validation studies over cropland for MOD15 collection 5 and GEOLAND-2 (GEOv1) products. The study area covers indeed main European crop types (wheat, maize, sunflower, soybean and rapeseed), and all crop phenological stages

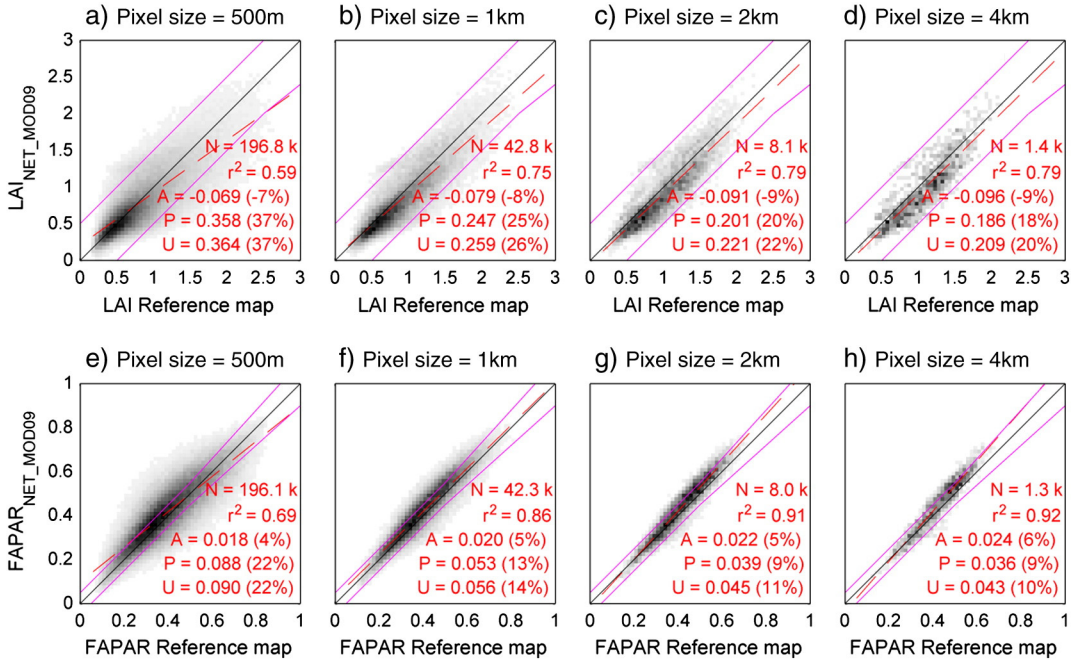

Fig. 12. Comparison of LAI and FAPAR reference maps with NET_MOD09 obtained at 500 m, 1 km, 2 km and 4 km. ECV estimates were derived from BV-NNET applied with MOD09 SR were aggregated from daily 500 m MOD09GA (Terra only). Red dashed line represents the overall fit and magenta lines the GCOS specifications boundaries. Magenta lines represent the GCOS (2011) specifications boundaries. Refer to Fig. 4 legend. (For interpretation of the references to color in this figure legend, the reader is referred to the web version of this article.)

were analyzed during 5 years of Formosat-2 data acquisition. With 474 CMG reference maps pixels used for the comparison, MOD15 yielded an uncertainty of 0.23 (23%) and 0.07 (18%) for LAI and FAPAR, respectively, with low biases. At the opposite, GEOv1 displayed systematic overestimations for LAI and FAPAR.

LAI/FAPAR estimates derived from BV-NNET tool applied on both MODIS sensors (on board of Aqua and Terra) data were very similar even when data were acquired and not corrected from different geometry. The confrontation of the BV-NNET estimates with the reference maps provided better agreement than MOD15 and GEOv1. The use of BRDF corrected SR as input of BV-NNET did not improve significantly the LAI estimates performances and the two outputs (LAI_{NET_MODN} and LAI_{NET_MOD09}) were highly correlated ($r^2 = 0.95$). These results suggested that BRDF effects are well taken into account both by VJB and PROSAIL models for vegetated covers. FAPAR estimated from non-BRDF-corrected SR ($FAPAR_{NET\_MOD09}$) were in good agreement with the reference maps but showed significant discrepancies with low winter values of FAPAR from BRDF-corrected SR ($FAPAR_{NET\_MODN}$) and $FAPAR_{MOD15}$. These discrepancies were attributed to various Lambertian soil properties modeling assumptions. Nonetheless, the four products displayed a good overall temporal consistency in agreement with the reference maps. The analysis of the time series noise highlighted that the two daily BV-NNET estimates were smoother than the 4-day composited MOD15 products.

This study was made in the context on the Land Product Validation as part of other similar studies (Fang et al., 2012; Garrigues et al., 2008; Weiss et al., 2007). Contrary to the mentioned studies, the current one aimed to validate LAI/FAPAR throughout time by combining in situ measurements and high spatial and temporal remote sensing time series data. Due to the limited availability of such data, the analysis was carried out over a unique crop site. This study showed that BV-NNET produced good results over cropland, but more investigations using a similar time series approach need to be carry over other land cover type (natural vegetation, grassland, savannah, different forest types). Previous studies have shown that the good agreement obtained with BV-NNET over crops was difficult to reproduce over more complex canopy such as forest. A second limitation concerns the resolution used for the comparison. It was shown that the errors decreased with the increase of the resolution due essentially to decrease of geometric effects. There was nonetheless a significant discrepancy between LAI and FAPAR GCOS specifications. According to the presented comparisons with BV-NNET products and MOD15, the LAI specification appeared indeed much more permissive than the FAPAR one. Finally, the method used to derive the MODIS and Formosat-2 LAI/FAPAR was based on the same BV-NNET tool. This may be a problem of the validation process as reference maps were validated on a limited number of field and crop types. In the future, a generalization of the approach described in this paper over the Joint Experiment of Crop Assessment and Monitoring network will include a larger number of crop types.

Acknowledgments

This paper includes Formosat-2 images which are material ©NSPO (2005–2006), distribution Astrium GeoInformation Services. All rights reserved. We are grateful to CNES (DCT/ME/EI) for the geometrical processing of the Formosat-2 images. We would like to thank the farmers for allowing us to make use of their fields for in situ measurements. We thank the two anonymous reviewers who provided helpful comments to improve the quality of the manuscript.

References

Bacour, C., Jacquemoud, S., Tourbier, Y., Dechambre, M., & Frangi, J. P. (2002). Design and analysis of numerical experiments to compare four canopy reflectance models. *Remote Sensing of Environment*, *79*, 72–83.

Baillarin, S., Gigord, P., & Hagolle, O. (2008). Automatic registration of optical images, a stake for future missions: Application to ortho-rectification, time series and mosaic products. In IEEE (Ed.), *IGARSS* (pp. 1112–1115) (Boston).

Baret, F., & Buis, S. (2008). Estimating canopy characteristics from remote sensing observations: Review of methods and associated problems. In S. Liang (Ed.), *Advances in land remote sensing* (pp. 173–201). Netherlands: Springer.

Baret, F., de Solan, B., Lopez-Lozano, R., Ma, K., & Weiss, M. (2010). GAI estimates of row crops from downward looking digital photos taken perpendicular to rows at 57.5 degrees zenith angle: Theoretical considerations based on 3D architecture models and application to wheat crops. *Agricultural and Forest Meteorology*, *150*, 1393–1401.

Baret, F., Hagolle, O., Geiger, B., Bicheron, P., Miras, B., Huc, M., et al. (2007). LAI, fAPAR and fCover CYCLOPES global products derived from VEGETATION — Part 1: Principles of the algorithm. *Remote Sensing of Environment*, *110*, 275–286.

Baret, F., Leroy, M., Hagolle, O., Bicheron, P., Roujean, J. L., Weiss, M. B. C., et al. (2004). Development of high level biophysical products from the fusion of medium resolution sensors for regional to global applications: The CYCLOPES project. *ENVISAT workshop (Salzburg, Austria)*.

Baret, F., Weiss, M., Lacaze, R., Camacho, F., Makhmara, H., Pacholcyzk, P., et al. (2013). GEOV1: LAI and FAPAR essential climate variables and FCOVER global time series capitalizing over existing products. Part1: Principles of development and production. *Remote Sensing of Environment*, *137*, 299–309, http://dx.doi.org/10.1016/j.rse.2012.12.027.

Béziat, P., Ceschia, E., & Dedieu, G. (2009). Carbon balance of a three crop succession over two cropland sites in South West France. *Agricultural and Forest Meteorology*, *149*, 1628–1645.

Bréon, F. -M., & Vermote, E. (2012). Correction of MODIS surface reflectance time series for BRDF effects. *Remote Sensing of Environment*, *125*, 1–9.

Bsaibes, A., Courault, D., Baret, F., Weiss, M., Olioso, A., Jacob, F., et al. (2009). Albedo and LAI estimates from FORMOSAT-2 data for crop monitoring. *Remote Sensing of Environment*, *113*, 716–729.

Camacho, F., Cernicharo, J., Lacaze, R., Baret, F., & Weiss, M. (2013). GEOV1: LAI, FAPAR essential climate variables and FCOVER global time series capitalizing over existing products. Part 2: Validation and intercomparison with reference products. *Remote Sensing of Environment*, *137*, 310–329, http://dx.doi.org/10.1016/j.rse.2013.02.030.

Chern, J. -S., & Wu, A. -M. (2004). Some aspects of ROCSAT-2 system engineering. *Acta Astronautica*, *54*, 145–151.

Claverie, M. (2012). Estimation spatialisée de la biomasse et des besoins en eau des cultures à l'aide de données satellitales à hautes résolutions spatiale et temporelle: Application aux agrosystèmes du sud-ouest de la France. *Université Paul Sabatier — Toulouse III* (pp. 228).

Claverie, M., Demarez, V., Duchemin, B., Hagolle, O., Ducrot, D., Marais-Sicre, C., et al. (2012). Maize and sunflower biomass estimation in southwest France using high spatial and temporal resolution remote sensing data. *Remote Sensing of Environment*, *124*, 844–857.

Cohen, W. B., & Justice, C. O. (1999). Validating MODIS terrestrial ecology products: Linking in situ and satellite measurements. *Remote Sensing of Environment*, *70*, 1–3.

Demarez, V., Duthoit, S., Baret, F., Weiss, M., & Dedieu, G. (2008). Estimation of leaf area and clumping indexes of crops with hemispherical photographs. *Agricultural and Forest Meteorology*, *148*, 644–655.

Deng, F., Chen, J. M., Plummer, S., Chen, M., & Pisek, J. (2006). Algorithm for global leaf area index retrieval using satellite imagery. *IEEE Transactions on Geoscience and Remote Sensing*, *44*, 2219–2229.

Duveiller, G., Weiss, M., Baret, F., & Defourny, P. (2011). Retrieving wheat Green Area Index during the growing season from optical time series measurements based on neural network radiative transfer inversion. *Remote Sensing of Environment*, *115*, 887–896.

Fang, H., Jiang, C., Li, W., Wei, S., Baret, F., Chen, J. M., et al. (2013). Characterization and intercomparison of global moderate resolution leaf area index (LAI) products: Analysis of climatologies and theoretical uncertainties. *Journal of Geophysical Research – Biogeosciences*, *118*, 529–548.

Fang, H., Wei, S., & Liang, S. (2012). Validation of MODIS and CYCLOPES LAI products using global field measurement data. *Remote Sensing of Environment*, *119*, 43–54.

Fisher, M., & Courtier, P. (1995). Estimating the covariance matrices of analysis and forecast error in variational data assimilationIn E. T. Memo (Ed.), .

Garrigues, S., Lacaze, R., Baret, F., Morisette, J. T., Weiss, M., Nickeson, J. E., et al. (2008). Validation and intercomparison of global Leaf Area Index products derived from remote sensing data. *Journal of Geophysical Research — Biogeosciences*, *113*, G02028.

GCOS (2006). Systematic observation requirements for satellite-based products for climate. *GCOS-107 (WMO/TD-No. 1338)*.

GCOS (2010). GCOS-13.: Implementation plan for the global observing system for climate in support of the UNFCCC (2010 update). *GCOS*, *138*. (pp. 186).

GCOS (2011). Systematic observation requirements for satellite-based products for climate. 2011 update. *GCOS-154*.

Gobron, N., Pinty, B., Aussedat, O., Chen, J. M., Cohen, W. B., Fensholt, R., et al. (2006). Evaluation of fraction of absorbed photosynthetically active radiation products for different canopy radiation transfer regimes: Methodology and results using Joint Research Center products derived from SeaWiFS against ground-based estimations. *Journal of Geophysical Research-Atmospheres*, *111*, D13110.

Gobron, N., & Verstraete, M. (2009a). ECV T10 fraction of absorbed photosynthetically active radiation (fAPAR). *Assessment of the status of the development of the standards for the terrestrial essential climate variables*. FAO.

Gobron, N., & Verstraete, M. (2009b). ECV T11 leaf area index (LAI). *Assessment of the status of the development of the standards for the terrestrial essential climate variables*. FAO.

Hagolle, O., Dedieu, G., Mougenot, B., Debaecker, V., Duchemin, B., & Meygret, A. (2008). Correction of aerosol effects on multi-temporal images acquired with constant viewing angles: Application to Formosat-2 images. *Remote Sensing of Environment*, *112*, 1689–1701.

Hagolle, O., Huc, M., Pascual, D.V., & Dedieu, G. (2010). A multi-temporal method for cloud detection, applied to FORMOSAT-2, VENμS, LANDSAT and SENTINEL-2 images. *Remote Sensing of Environment*, *114*, 1747–1755.

ICRAF-ISRIC (2010). A globally distributed soil spectral library: Visible near infrared diffuse reflectance spectra. World Agroforestry Centre (ICRAF) and ISRIC — World soil information. Available on: http://africasoils.net/data/ICRAF-ISRICspectra

Jacquemoud, S., Bacour, C., Poilve, H., & Frangi, J. P. (2000). Comparison of four radiative transfer models to simulate plant canopies reflectance: Direct and inverse mode. *Remote Sensing of Environment*, *74*, 471–481.

Jacquemoud, S., & Baret, F. (1990). PROSPECT — A model of leaf optical-properties spectra. *Remote Sensing of Environment*, *34*, 75–91.

Jacquemoud, S., Verhoef, W., Baret, F., Bacour, C., Zarco-Tejada, P. J., Asner, G. P., et al. (2009). PROSPECT plus SAIL models: A review of use for vegetation characterization. *Remote Sensing of Environment*, *113*, S56–S66.

Jonckheere, I., Fleck, S., Nackaerts, K., Muysa, B., Coppin, P., Weiss, M., et al. (2004). Review of methods for in situ leaf area index determination. Part I. Theories, sensors and hemispherical photography. *Agricultural and Forest Meteorology*, *121*, 19–35.

Knyazikhin, Y., Glassy, J., Privette, J. L., Tian, Y., Lotsch, A., Zhang, Y., et al. (1999). MODIS leaf area index (LAI) and fraction of photosynthetically active radiation absorbed by vegetation (FPAR) product (MOD15) algorithm theoretical basis document. Available on: http://modis.gsfc.nasa.gov/data/atbd/atbd_mod15.pdf

Knyazikhin, Y., Martonchik, J. V., Myneni, R. B., Diner, D. J., & Running, S. W. (1998). Synergistic algoritm for estimating vegetation canopy leaf area index and fraction of absorbed photosynthetically active radiation from MODIS and MISR data. *Journal of Geophysical Research-Atmospheres*, *103*(D24), 32257–32276.

Mather, P.M., & Koch, M. (2010). *Computer processing of remotely-sensed images: An introduction.*

McCallum, I., Wagner, W., Schmullius, C., Shvidenko, A., Obersteiner, M., Fritz, S., et al. (2010). Comparison of four global FAPAR datasets over Northern Eurasia for the year 2000. *Remote Sensing of Environment*, *114*, 941–949.

Morisette, J. T., Baret, F., Privette, J. L., Myneni, R. B., Nickeson, J. E., Garrigues, S., et al. (2006). Validation of global moderate-resolution LAI products: A framework proposed within the CEOS land product validation subgroup. *IEEE Transactions on Geoscience and Remote Sensing*, *44*, 1804–1817.

Myneni, R. B., Hoffman, S., Knyazikhin, Y., Privette, J. L., Glassy, J., Tian, Y., et al. (2002). Global products of vegetation leaf area and fraction absorbed PAR from year one of MODIS data. *Remote Sensing of Environment*, *83*, 214–231.

Rembold, F., Atzberger, C., Savin, I., & Rojas, O. (2013). Using low resolution satellite imagery for yield prediction and yield anomaly detection. *Remote Sensing of Environment*, *5*, 1704–1733.

Running, S. W., Baldocchi, D.D., Turner, D. P., Gower, S. T., Bakwin, P.S., & Hibbard, K. A. (1999). A global terrestrial monitoring network integrating tower fluxes, flask sampling, ecosystem modeling and EOS satellite data. *Remote Sensing of Environment*, *70*, 108–127.

Sedano, F., Lavergne, T., Ibañez, L. M., & Gong, P. (2008). A neural network-based scheme coupled with the RPV model inversion package. *Remote Sensing of Environment*, *112*, 3271–3283.

Verger, A., Baret, F., & Camacho, F. (2011). Optimal modalities for radiative transfer-neural network estimation of canopy biophysical characteristics: Evaluation over an agricultural area with CHRIS/PROBA observations. *Remote Sensing of Environment*, *115*, 415–426.

Verhoef, W. (1984). Light-scattering by leaf layers with application to canopy reflectance modeling — The SAIL model. *Remote Sensing of Environment*, *16*, 125–141.

Vermote, E. F., El Saleous, N. Z., & Justice, C. O. (2002). Atmospheric correction of MODIS data in the visible to middle infrared: First results. *Remote Sensing of Environment*, *83*, 97–111.

Vermote, E., Justice, C. O., & Breon, F. M. (2009). Towards a generalized approach for correction of the BRDF effect in MODIS directional reflectances. *IEEE Transactions on Geoscience and Remote Sensing*, *47*, 898–908.

Vermote, E. F., & Kotchenova, S. (2008). Atmospheric correction for the monitoring of land surfaces. *Journal of Geophysical Research-Atmospheres*, *113*, D23S90.

Vohland, M., Mader, S., & Dorigo, W. (2010). Applying different inversion techniques to retrieve stand variables of summer barley with PROSPECT and SAIL. *International Journal of Applied Earth Observation and Geoinformation*, *12*, 71–80.

Walthall, C., Dulaney, W., Anderson, M., Norman, J., Fang, H., & Liang, S. (2004). A comparison of empirical and neural network approaches for estimating corn and soybean leaf area index from Landsat ETM + imagery. *Remote Sensing of Environment*, *92*, 465–474.

Weiss, M. (1998). Développement d'un algorithme de suivi de la végétation à large échelle. *Université de Sophia Antipolis* (pp. 188).

Weiss, M., Baret, F., Smith, G. J., & Jonckheere, I. (2004). Methods for in situ leaf area index measurement, part II: From gap fraction to leaf area index: Retrieval methods and sampling strategies. *Agricultural and Forest Meteorology*, *121*, 17–53.

Weiss, M., Baret, F., Garrigues, S., & Lacaze, R. (2007). LAI and fAPAR CYCLOPES global products derived from VEGETATION. Part 2: Validation and comparison with MODIS collection 4 products. *Remote Sensing of Environment*, *110*, 317–331.

Widlowski, J. L., Robustelli, M., Disney, M., Gastellu-Etchegorry, J. P., Lavergne, T., Lewis, P., et al. (2008). The RAMI on-line model checker (ROMC): A web-based benchmarking facility for canopy reflectance models. *Remote Sensing of Environment*, *112*, 1144–1150.